Article

Simultaneous electrocatalytic CO2 reduction and enhanced electrochromic effect at WO3 nanostructured electrodes in acetonitrile

Néstor E. Mendieta-Reyes, Ana Korina Díaz-García, and Roberto Gómez

ACS Catal., **Just Accepted Manuscript** • DOI: 10.1021/acscatal.7b03047 • Publication Date (Web): 12 Jan 2018

Simultaneous electrocatalytic CO_2 reduction and enhanced electrochromic effect at WO_3 nanostructured electrodes in acetonitrile

Néstor E. Mendieta-Reyes[ab], Ana Korina Díaz-García[b], Roberto Gómez[b]

[a] *Departamento de Química, Facultad de Ciencias, Universidad Nacional de Colombia, Cra 30 # 45-03, Edificio 451, Bogotá, Colombia.*

[b] *Institut Universitari d' Electroquímica i Departament de Química Física, Universitat 'dAlacant, Apartat 99, E-03080 Alicante, Spain.*

ABSTRACT

Serious concerns about the climate change make particularly attractive the reutilization of CO_2, being one option the electroreduction of CO_2 in acetonitrile solutions on a range of electrode materials. Among them, transition metal oxides stand out as cost effective alternatives. In this context, the electrocatalytic activity of nanostructured WO_3 electrodes for carbon dioxide reduction in both humid and dry acetonitrile media has been addressed by using electrochemical and spectroelectrochemical measurements. Importantly the cathodic faradaic process starts at potentials as high as -0.16 V vs SHE. Gas chromatography measurements show CO as being the main product in both dry and humid acetonitrile, together with formate in the presence of humidity. Interestingly, purging with CO_2 not only causes the appearance of cathodic faradaic currents, but also an increase in capacitive currents, which are directly associated with an enhanced electrochromic effect. The ICP-MS determination of tungsten upon electrolysis confirms a minor electrodissolution of WO_3 electrode. On the basis of these observations, a mechanism is proposed in which WO_3 is not only the electrode material, but also a mediator in the CO_2 reduction process

KEYWORDS: CO_2 reduction, CO_2 activation, Electrochromic effect, spectroelectrochemistry, electrodissolution, WO_3 electrodes.

1. INTRODUCTION

The current atmospheric levels of carbon dioxide and the depletion of fossil fuel reserves raise serious concerns about the resulting effects on the global climate change and on the future of some energy sources. Carbon dioxide reduction to fuels such as methane or methanol is a potential way to address both problems simultaneously, as it provides a means of recycling CO_2 and obtaining fuels (energy storage). However, the CO_2 molecule is stable, with a closed-shell electronic configuration, and a linear geometry.[1] A single electron transfer causes a partial sp^2 hybridization of the carbon atom and a bending of the molecular structure due to the repulsion between the electron added to the electrophilic carbon atom and the free electron pairs at the oxygen atoms. Indeed, the LUMO of CO_2 is strongly antibonding with respect to the C-O bonds. Both the loss of symmetry and the increased repulsion between the electron clouds in the bent structure (with distortion of the linear $D_{\infty h}$ geometry) contribute to the high energy barrier of the first electron transfer[2] ($CO_2 + e^- \rightarrow CO_2^{\cdot -}$). Thermodynamically, the first electron transfer requires potentials more negative than −1.97 V vs SHE in an aprotic solvent such as (DMF),[3] or −1.90 V vs SHE in water.[4,5] In this respect, the adsorption of CO_2 on semiconductor surfaces offers a way of activating the inert molecule for reduction, because adsorption has been reported to lead to the formation of a partially charged species ($CO_2^{\delta\cdot -}$) through interactions with surface atoms.[2] In fact, the lower the O–C–O bond angle, the higher the partial charge density of the $CO_2^{\delta\cdot -}$as concluded from different spectroscopic techniques.[6,7] In addition, in the carbon dioxide molecule, the carbon atom is in its highest oxidation state and the reduction reaction can proceed through the exchange of two, four, six, and eight electrons per C atom through different pathways. This fact suggests that the CO_2 reduction and the product distribution strongly depend on the reaction conditions; electrode material,[8] surface structure,[1] applied potential, electrolyte,[9]

type of solvent (aqueous vs nonaqueous and protic vs aprotic) among others. A wide variety of products with different oxidation states ranging from $C_2O_4^{2-}$ to CH_4 and other hydrocarbons have been reported.[10–16]

The CO_2 reduction has been investigated by using different approaches, such as those of (photo) electrocatalysis,[17] photocatalysis[18,19] and homogeneous catalysis.[20] The homogeneous process is usually catalyzed by metal complexes with the disadvantage that it relies primarily on rare and expensive metals such as ruthenium or rhenium.[21] Transitions metals and their compounds, such as metal oxides, are used as photocatalysts for CO_2 reduction.[22] In fact, these materials have active electrons and vacant d orbitals, which are able to induce the activation of the CO_2 molecule not only by adduct formation, but also facilitating the desorption of the reduction products.[2] In this sense, WO_3 has been used as a photocatalyst for CO_2 reduction,[23] although it has thermodynamic limitations because the conduction band edge corresponds to a less reductive potential (-0.1 V vs SHE at pH=7) than necessary for the first electron transfer to CO_2 ($CO_2/CO_2^{\cdot-}$ couple).

WO_3 is an interesting material which exhibits a large variety of useful properties for different technological applications due to its capability of sustaining structural transformations with changes in the optical properties, which is critical for technologies such as displays and smart windows. However, these properties strongly depend on the morphology of the material. It is worth noting that WO_3 is probably the most studied electrochromic material as it can be reduced either chemically or electrochemically to form intensely colored compounds known as tungsten bronzes.[24] The electrochromic properties of WO_3 films are based on the simultaneous injection of electrons to the conduction band or surface states and the intercalation of small cations from

solution. However, with large cations whose intercalation is not possible, other processes such as lattice polarization, dissociative reduction and electrodissolution eventually can occur. In this respect, an interesting model about electrochromism with large cation has been proposed by Hepel and coworkers.[25]

When CO_2 reduction is carried out in aqueous media, proton reduction becomes an important parallel reaction. In addition, in aqueous media, CO_2 solubility is relatively low, leading to diffusion limitations. Using nonaqueous aprotic solvents, such as acetonitrile (ACN), is convenient because they provide a wider electrochemical window, suitable for the observation of CO_2 reduction. Also, the solubility of CO_2 in ACN is 270 mM at atmospheric pressure and room temperature, which is eight times that in water.[26] The aim of this paper is to show a study of the carbon dioxide reduction on WO_3 electrodes with two different nanostructures (nanoparticles and nanorods) in ACN media by means of electrochemical and spectroelectrochemical measurements. These measurements have been done in the absence and in the presence of water. In both cases, an enhanced capacitive behavior accompanies CO_2 reduction. In addition, CO_2 reduction is accompanied by a slight electrodissolution of WO_3. The implications of these observations in the CO_2 reduction mechanism are analyzed.

2. MATERIALS AND METHODS

2.1 WO_3 electrode preparation

WO_3 nanoparticulate thin films (identified as NP) were prepared on FTO substrates by spin-coating followed by a two-step thermal treatment. WCl_6 (150 mg, purity 99.99%+, Aldrich Chem. Co.) and polyethylene glycol (25 mg, purity 99%, Aldrich Chem. Co.) were dissolved in 1.25 mL ethanol and stirred for 4 hours.[27] Then, this precursor was spin-coated onto FTO at 1500

rpm for 15 s. The samples were dried at 40 ºC in air for 30 minutes and then annealed at 500 ºC for 30 minutes.

A solvothermal technique was used to grow WO_3 nanorod films (identified as NR) on FTO coated glass.[28] WO_3 nanorod growth was assisted by a WO_3 seed layer, which was prepared by dissolving 1.25 g of tungstic acid (H_2WO_4, Alfa Aesar Johnson Matthey GmbH, 99%), 0.5g of poly(vinyl alcohol) ([-CH_2CHOH-] Alfa Aesar Johnson Matthey GmbH, 98 – 99 %) in 10 mL of 50 wt % hydrogen peroxide solution (H_2O_2, Panreac, 33%). After 1h, this precursor was spin-coated onto FTO at 4000 rpm for 30 s. The samples were air dried followed by an annealing process at 500 °C for 2 h in air. For the nanorod array film deposition, the substrate (supporting a seed layer) was vertically placed in an autoclave filled with 3 mL of H_2WO_4 aqueous solution (0.05 M), 9 mL of ethanol (CH_3CH_2OH, GPR Rectapur 96% vol), 4 mL of 6 M HCl (HCl, Fluka 37%), 0.01 g of oxalic acid (HO_2CCO_2H, R.P. normapurtm AR), and 0.02 g of urea (NH_2CONH_2, Sigma-Aldrich puriss. p.a., ACS reagent). The autoclave was then sealed and maintained at 180 °C for 24 h. Then, the substrate was rinsed with deionized water and annealed in air at 500 °C for 2 h.

2.2 Structural, morphological, electrochemical and spectroelectrochemical measurements

A Bruker D8-Advance X-ray diffractometer operating with Cu-Kα radiation (λ=0.154 nm) at 40 kV and 40 mA was used to determine the X-ray diffraction pattern of the films. The surface morphology was analyzed using the JEOL JEM-1400 field emission scanning electron microscope (FE-SEM).

Electrochemical measurements were performed at room temperature using a conventional three-electrode cell and a computer-controlled Autolab PGSTAT30 potentiostat. In all the cases

a Pt wire was employed as a counter electrodeThe reference electrode was a $Ag/AgCl_{(s)}/KCl_{(sat)}$ electrode. Unless otherwise stated all the potentials are quoted versus this reference. Also, in the Supplementary data, details on the conversion of potentials measured against Ag/AgCl(s)/KCl(aq) to the SHE scale are given. The supporting electrolyte was 0.1 M tetrabutylammonium perchlorate (TBAP; ≥99.0%, Sigma-Aldrich for electrochemical analysis) in ACN (99.88% anhydrous from Scharlau, Multisolvent, HPLC grade), with a water content of 530 ppm as determined by Karl Fisher titration. Cyclic voltammetry was carried out in the dark at a scan rate of 50 mVs^{-1}.

Spectroelectrochemical measurements were performed by coupling an electrochemical cell to a UV−vis spectrophotometer (UV-2401 PC Shimadzu). The cell employed for the spectroelectrochemical measurements was equipped with a cuvette fitted at its bottom and mounted on the support of the spectrophotometer sample chamber. The reference and the counter electrode are the same as in the case of the conventional electrochemical cell described above. The experiments were conducted by coupling chronoamperometric/chronopotentiometric measurements at several potentials with absorbance versus time measurements at a fixed wavelength.

In order to evaluate the water effect in the supporting electrolyte, ACN was dried with a 3A molecular sieve (rods from Sigma-Aldrich) for 72 h in a glove box following a reported procedure, leading to a water content below 10 ppm.[29] In all the experiments, the electrolyte was purged with either N_2 or CO_2 gas for 30 min using an ACN trap to prevent solvent evaporation.

2.3 Analytical procedures

Experiments were carried out in a closed and sealed glass cell with two compartments separated by a Nafion TM membrane NM-117. The Nafion membrane was boiled in 3% (v/v) H_2O_2 for 1 h, and then in distilled water for another hour. Then the membrane was boiled in 0.5 M H_2SO_4 for 1 h, followed anew by boiling in distilled water for 1 h, and finally dried with a nitrogen flow before use for removing organic impurities.[30] The working electrode was an electrochemically pretreated nanoparticulate WO_3-NP/FTO electrode (4 cm^2 of geometric area) and an Ag/AgCl(s)/$KCl_{(aq)}$ was used as a reference electrode. Unless otherwise stated all the potentials are quoted versus this reference. A platinum wire was placed in the counter electrode compartment. Both compartments were filled with CO_2-purged 0.1 M TBAP in either wet or dry ACN, and the cell was closed by sealing the joints with silicone. A potentiostatic electrolysis was made at -1.2 V for humid conditions and -1.5 V for dry conditions for 1.5 h in both cases. Samples of 250 μL were extracted from the headspace of the working electrode compartment and analyzed with a Hewlett-Packard 5890 gas chromatograph equipped with a thermal conductivity detector. In addition, samples of 1.0 mL of the working solution were collected in 300μl of deionized water as to dissolve possible products into the water/ACN mixture, allowing their detection. For ionic chromatography detection, a 883 Basic IC plus ion chromatograph equipped with an injection loop of 20 μL, a polymethacrylate–based column (75 x 4.6 mm, Metrosep Dual 2, Metrohm) and a chemical conductivity suppressor (50 mM H_2SO_4) were employed. A constant flow of 1.0 mL/min was utilized. The eluent was a solution 9.0 mM in Na_2CO_3 and 2.5 mM in $NaHCO_3$ for oxalate and formate determination, and citric acid 2.0mM + 0.01 phthalic acid for carbonate determination.[31]

The tungsten present in the solution upon the electrolysis was detected by Inductively coupled plasma – mass spectroscopy measurements (ICP-MS) whith a Thermo Elementa VGPQ-ExCell

spectrometer. A sample of 22 mL of the electrolytic solution was heated to 60ºC, in order to evaporate the acetonitrile. then, the tungsten contained in the residue was extracted with 4 mL 2% HNO_3 aqueous solution and 1 mL of 30% H_2O_2 in an ultrasonic bath. Finally, the sample was filtered using a nylon fiter (0.45µm pore diameter) and the final volume was adjusted to 5 mL with ultrapure water.

3. RESULTS

3.1 Electrode characterization

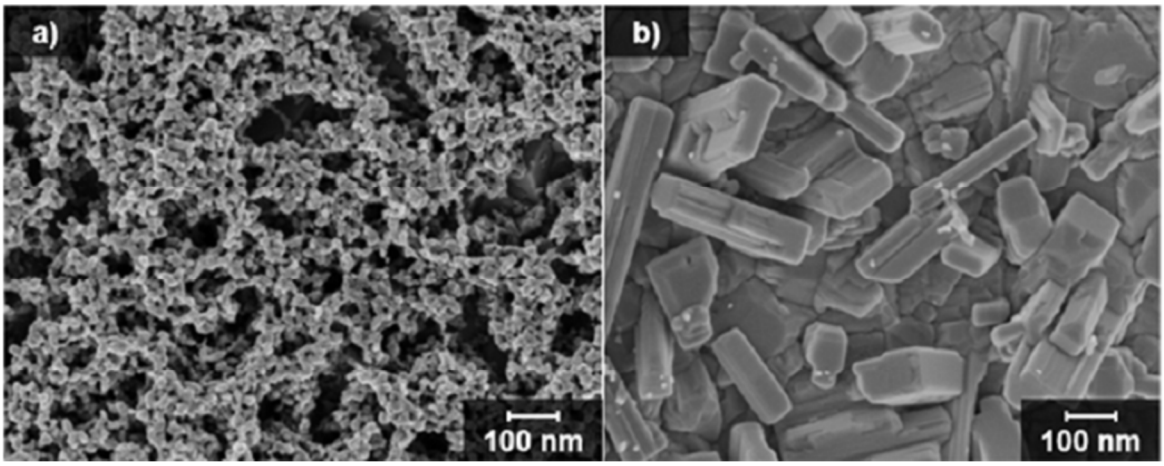

Figure 1. FESEM images of WO3 nanostructures coated on FTO conducting glass and prepared following two different routes of synthesis, a) nanoparticles via a sol-gel technique and b) nanorods via a hydrothermal technique.

Thin film WO_3 electrodes were coated on FTO substrates following two different synthesis routes as explained above leading to different morphologies. Figure 1 shows FE-SEM micrographs for WO_3-NP electrodes obtained by sol-gel (Figure 1a) and WO_3-NR electrodes obtained by a hydrothermal method (Figure 1b). The morphology of the film surface of WO_3-NP shows that nanocrystals are well distributed on the surface and connected to one another. Grains

have an average diameter of 10 nm. The WO_3-NR electrodes grow up in a random orientation with nanorods 80-100 nm in diameter and 500 nm in length. To verify the structure of the as-prepared thin films (including a thermal treatment in air), they were analyzed by XRD. Figure S1 shows that both sol-gel and solvothermal synthetized WO_3 correspond to the monoclinic phase (compared with JCPDS 01-072-0677), which was the only phase detected.[32] Two characteristic triplets of WO_3 consisting of (002), (020), (200) and (022), (202), (202) reflections are seen in the diffraction angle range of 22.5-24.7º and 33-34.5º, respectively. The (200), (020), and (002) faces, indicate that the as-prepared product presents high-crystallinity.

3.2 Electrochemical studies

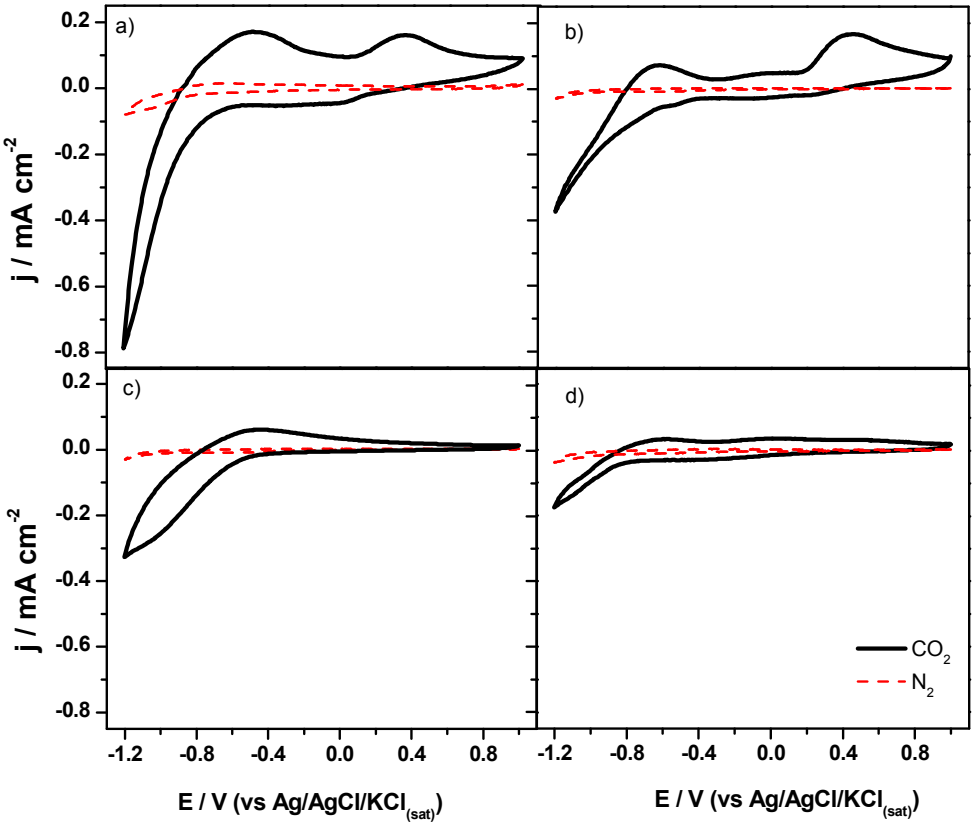

Figure 2. Cyclic voltammograms for WO_3 electrodes in 0.1 M TBAP/acetonitrile. Black and red curves correspond to the electrolyte purged with CO_2 and N_2, respectively; a) and b) WO_3 -NP and WO_3-NR in humid acetonitrile respectively; c) and d) WO_3-NP and WO_3-NR in dry acetonitrile, respectively.

The electrochemical studies were performed in two steps. First, the effect of the morphology was evaluated with thin film electrodes formed by either nanoparticles or nanorods, using a supporting electrolyte prepared in humid ACN (Figures 2a y 2b). Second, the same morphologies were used, but the supporting electrolyte was prepared in ACN with a drying pretreatment (procedure described above) to evaluate the effect of water in the medium (Figure 2c y 2d). Figures 2a and 2b show the voltammograms for WO_3-NP and WO_3-NR respectively using as received ACN as a solvent. First, the potential window for CO_2 reduction was determined by purging with N_2. In a nitrogen atmosphere, both WO_3-NP and WO_3-NR electrodes show an increase in the cathodic current with an onset at around -0.2 V, which coincides with the beginning of the accumulation region. From a chemical point of view, such a region can be seen as corresponding to W(VI)/(V) surface redox processes, analogous to the behavior observed in semiconductor materials such as TiO_2.[33] The W^{5+} species can be stabilized by small cations such as H^+ or Li^+ through intercalation processes (local formation of bronzes). Nevertheless, in our case, a voluminous cation tetrabutylammonium ($TBAP^+$) was used, and stabilization of W(V) surface centers (with high electronic density) is not efficient.

When the system was saturated with CO_2 during 30 min, a drastic increase in the cathodic current with an onset at -0.7V (-0.16V vs SHE)[34] was observed, evincing CO_2 reduction. Importantly, the onset of carbon dioxide reduction roughly coincides with the beginning of the WO_3 accumulation region (W^{6+} reduction) which is related to the location of the WO_3

conduction band edge. In this way, we may hypothesize that the accumulation of charge in surface states by the formation of W^{5+} species that act as electron rich centers for CO_2 reduction is necessary. It is important to note that carbon dioxide reduction does not proceed when a bare FTO conducting glass electrode is used (Figure S2), which confirms that the WO_3 surface has an electrocatalytic role, decreasing the potential requirements for carbon dioxide reduction. Linear scan voltammograms at a relatively slow scan rate (5 $mV \cdot s^{-1}$) were also recorded in the presence and in the absence of CO_2, providing further evidence on the faradaic nature of the cathodic currents linked to CO_2 reduction (Figure S3).

Many authors have attributed a decrease in the CO_2 reduction overpotential to an activation process induced by CO_2 adsorption and a subsequent bending of the molecule. The adsorption of CO_2 on metal oxide surfaces offers a way of activating the molecule with the formation of partially charged species ($CO_2^{\delta\cdot-}$).[35,36] In the CO_2 molecule, the oxygen atoms have free pairs of electrons that can be donated to Lewis acid surface centers, such as oxygen vacancies, forming carbonate-like species. The carbon atom could also gain electrons from Lewis base centers such as oxygen surface atom species. Additionally, the (C–O) π-electrons can also participate in reactions with surface centers such as W^{5+}, which could act as catalytic sites with high electronic density, inducing a lower O–C–O bond angle and decreasing the CO_2 LUMO level through electron density donation to the CO_2 molecule. It is worth mentioning that a decrease of 0.14 eV in the energy of the LUMO level with O-C-O angle of 170° has been reported.[1,2]

The surface morphology of the metal oxide plays an important role since it has catalytic sites, such as oxygen vacancies, stoichiometric defects, and grain edges whose nature and density depend on the exposed facets. In the same way, the average particle size is expected to have a dramatic effect on the specific interfacial area of the electrodes. These areas for both WO_3-NR

and WO_3-NP electrodes were evaluated using CV measurements in aqueous 0.1 M $HClO_4$ purged with N_2 (Figure S4). The voltammograms show a charge accumulation region in both cases. Clearly, in the WO_3-NP electrode, the accumulation region is larger than for WO_3-NR electrode. An evaluation of charge density in the accumulation region from the integration of the area below the curve in the voltammograms shows that the ratio of interfacial areas WO_3-NP/ WO_3-NR has a value of three. As expected, faradaic cathodic currents related to CO_2 reduction for the WO_3-NP are higher than for WO_3-NR.

Electrochemical experiments with dry ACN were also carried out with the aim of establishing the water trace effect. Many studies in non-aqueous media and ionic liquids have shown strong water content dependence and different pathways for CO_2 reduction that are not fully understood yet.[37–39] The behavior of water as a proton source in non-aqueous media can result in different CO_2 reduction final products (methanol or methane formation needs a proton source).

In fact, as shown in figures 2c and 2d, under dry conditions the cathodic currents associated with CO_2 reduction are significantly lower, which evinces a beneficial effect of water traces in ACN for CO_2 reduction. In addition, the peak at 0.4 V in the positive-going scan is no longer present. In this respect, Ramesha et al. using a TiO_2 electrode reported that an increase in water content in ACN (0.33 M) raises faradaic efficiency for methanol formation.[40] In this case, results show that CO_2 reduction in ACN electrolytes is highly sensitive to even trace amounts of water, regarding both the products obtained and, most likely, the reaction path through which they are formed. Figure S5 shows the chronoamperograms for a WO_3-NP electrode at a potential value of -1.0 V for 300 s where humid ACN gives larger CO_2 currents in agreement with the voltammetric results.

On the other hand, when water is present in the electrolyte, changes in pH in the vicinity of the electrode and in the bulk of the solution could be expected, promoted by the acid-base equilibrium between CO_2 and water, according to:

$$CO_{2(CH_3CN)} + H_2O_{(CH_3CN)} \leftrightharpoons HCO_{3\,(CH_3CN)}^{-} + H^+ \qquad (1)$$

where $H_2O_{(CH_3CN)}$ corresponds to water traces in ACN. These equilibria have been considered in an extensive study by Matsubara et al. A p*Ka* value of 23.4 for reaction 1 has been reported.[41] This value of p*Ka* corresponds to a low concentration of protons in the medium, mainly due to the low capacity of ACN to solvate anions. A hypothesis is that these changes in proton concentration can induce an intercalation of protons in the WO_3 lattice.

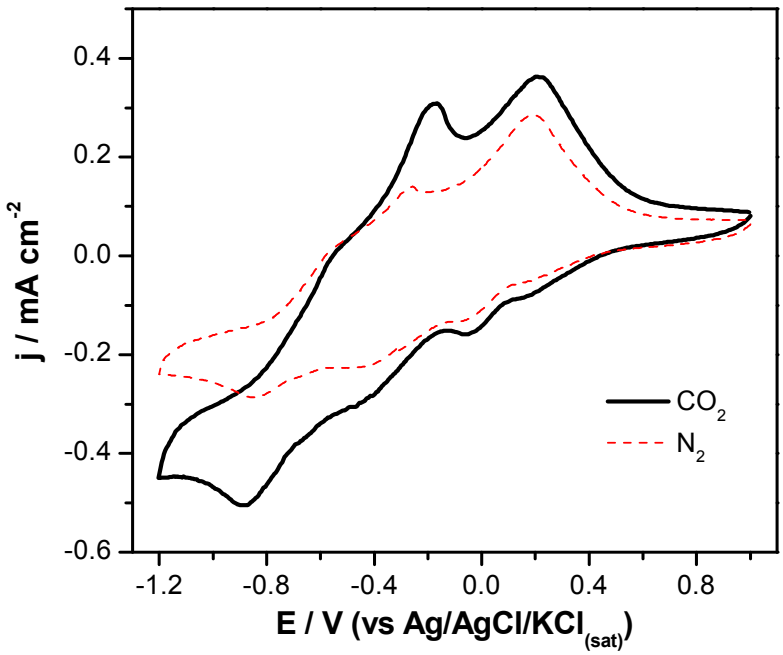

Figure 3. Cyclic voltammograms for a WO_3-NP electrode in 0.1 M TBAP + 2 mM methanesulfonic acid /acetonitrile. Black and red curves correspond to the electrolyte purged with either CO_2 or N_2, respectively.

In order to discard the presence of a substantial concentration of proton, an experiment was also carried out in which 2 mM methanesulfonic acid as proton source was added to dry ACN. A pK_a value of 9.97 has been calculated for this acid in ACN.[42] We found that in an N_2-purged solution, typical peaks related to the reversible formation of tungsten bronze appear in the voltammogram. Furthermore, upon purging with CO_2, an increase in the cathodic current and an increase in the currents related to the oxidation of the tungsten bronze are apparent (Figure 3). This supports the notion that the interaction of CO_2 with the surface causes an increase in the concentration of W^{5+}species in WO_3.

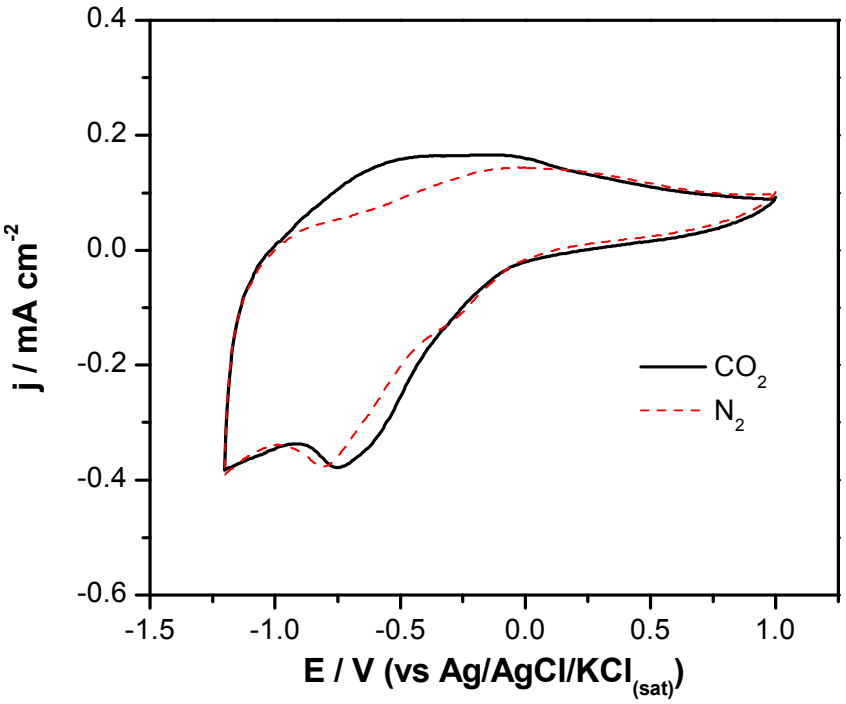

Figure 4. Cyclic voltammograms for a WO_3-NP in 0.1 M $LiClO_4$/acetonitrile. Black and red curves correspond to the electrolyte purged with CO_2 and N_2, respectively.

Figure 4 shows CVs under both N_2 and CO_2, typical for Li intercalation. No cathodic currents associated with CO_2 reduction are observed. It is well known that lithium can be adsorbed and

intercalated in the WO_3 lattice, acting as a blocking agent for the CO_2 activation sites (see below). In addition, Li^+ cations can stabilize W^{5+}. Another evidence is the electrochromic effect due to the intercalation of small cations Li^+. When the Li^+ cation is present in the supporting electrolyte, an intense blue coloration is observed in both N_2 and CO_2 purged solutions. At this point, the above electrochemical results show that several factors play a role in CO_2 reduction on WO_3, i) activation of CO_2 via adduct formation ($CO_2^{\delta\cdot-}$) facilitated by adsorption on WO_3, ii) catalytic sites with electron rich centers favoring first electron transfer. It is worth nothing that the adsorption of CO_2 on the surface not only induces the activation but it also favors pseudocapacitive processes associated to an enhanced electrochromic effect. In the following UV/vis spectroelectrochemical measurements to follow the W^{5+} density in WO_3 are shown.

3.3 UV/vis Spectroelectrochemical study

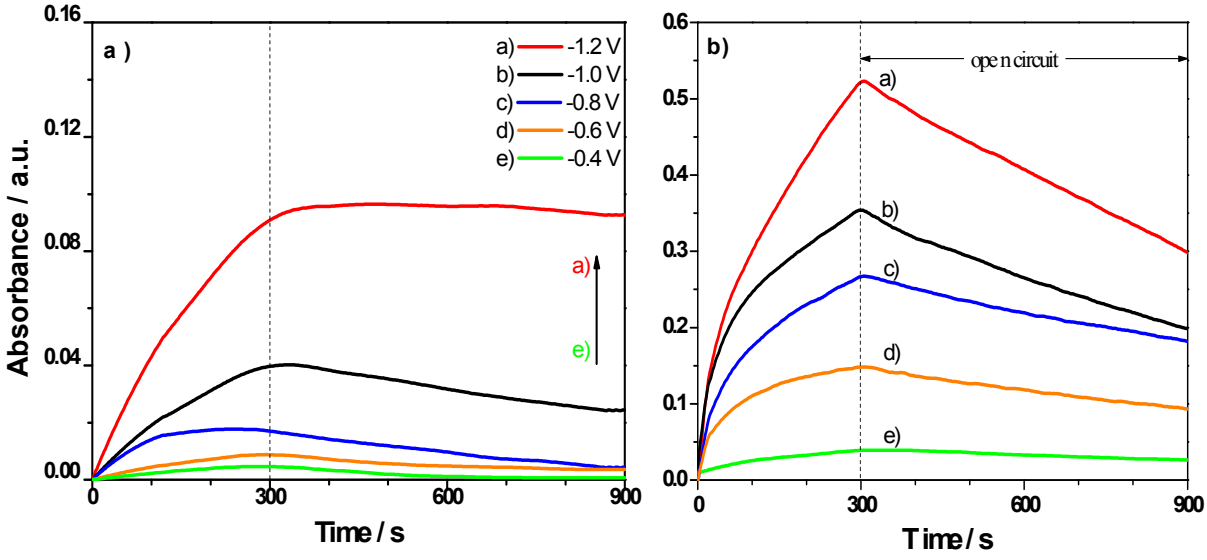

Figure 5. Absorbance at 680 nm vs time for an FTO/WO_3NR electrode in 0.1 M TBAP/ acetonitrile purged with (a) N_2 and (b) CO_2. Applied potential varied between -1.2 V to -0.4 V.

In situ UV/vis spectroelectrochemical experiments were carried out for monitoring the W^{5+} density in WO_3-NP films in a 0.1 M TBAP solution prepared with humid acetonitrile. The electrode was polarized at different potentials from -0.4 V to -1.2 V for 300 s, followed by 600 s at open circuit potential, under either N_2 or CO_2 atmospheres. Figure S6 shows typical absorption spectra when the electrode was polarized at different potentials. As revealed by the spectra, the WO_3 thin film electrodes display a high contrast between the bleached to colored states, being the coloration more intense for increasingly negative applied potentials. In addition, a broad peak is observed at 680nm in the spectra. The variation of absorbance versus time was recorded at this wavelength value (Figure 5). According to the intervalence charge transference model for electrochromism, the injected electrons are localized on W^{6+} ions to form W^{5+}, and the coloration is due to a transfer of electrons from W^{5+} to the WO_3 conduction band. However, there is still controversy about the detailed coloration mechanism.[43] Under an N_2 atmosphere the electrochromic effect is not strong and the increase in absorbance value is modest (Figure 5a). It is worth nothing that the use of voluminous cations, such as TBA^+, does not allow intercalation due to steric hindrance and a different mechanism for the electrochromic effect, including electrodissolution has been considered.[25]

In a CO_2-purged solution, values of absorbance higher than for N_2-purged solutions are consistently found, even at potentials where CO_2 reduction does not proceed (Figures 5b and S5). These spectroelectrochemical results are in agreement with those obtained by means of cyclic voltammetry in wich an increase in capacitance is evident when the electrolyte is saturated with CO_2, even at potentials where CO_2 reduction does not take place.

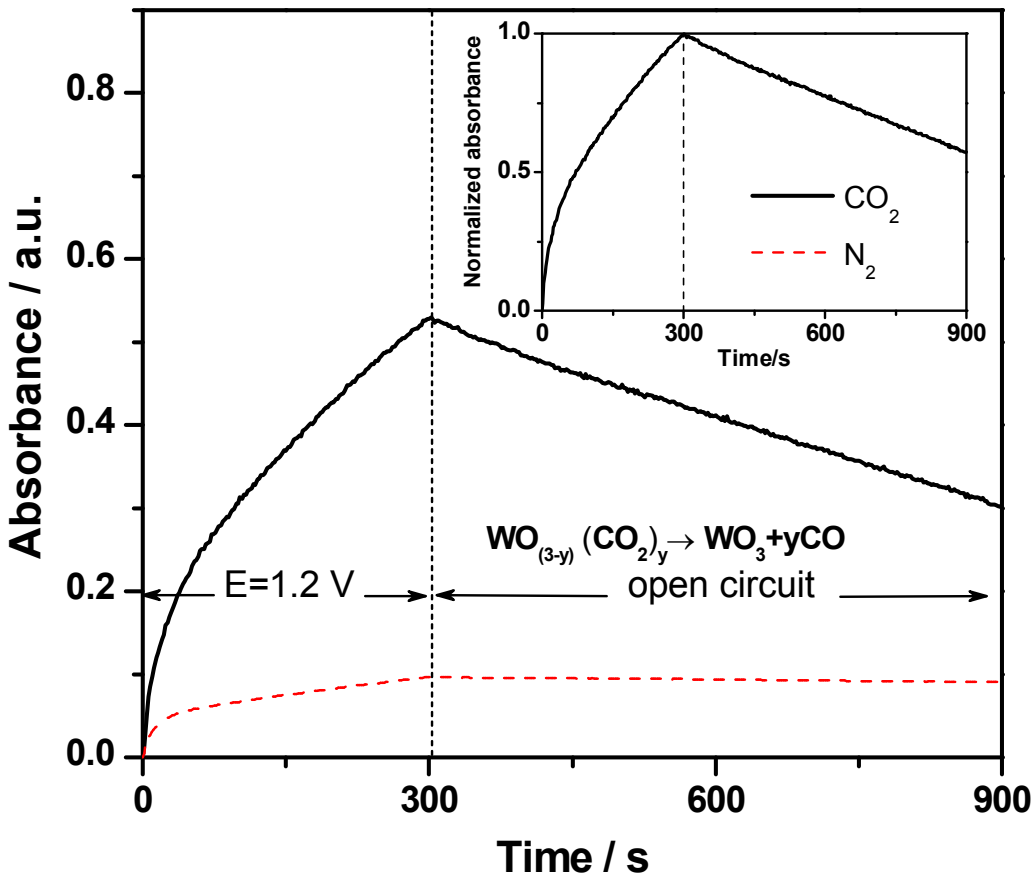

Figure 6. Absorbance at 680 nm vs time for FTO/WO_3-NR electrodes in 0.1 M TBAP/acetonitrile solutions, purged with either N_2 (red) or CO_2 (black) for 30 min. First, a potential of -1.2 V was applied for 300 s. Then, OC conditions were maintained for 600 s. Inset: normalized absorbance.

Figure 6 shows the absorbance versus time profiles for an applied potential of -1.2 V for 300 s in solutions purged with either N_2 or CO_2. After the potentiostatic control period, the electrode is maintained at open circuit for 600 s and the absorbance is observed to decrease with time. Under potentiostatic control, the maximum absorbance value for the system saturated with CO_2 is approximately 5 times larger than that obtained with N_2.

3.4 Determination of CO_2 reduction products.

Electrochemical CO_2 reduction products under both dry and humid conditions were determined through GC-TCD and ion chromatography upon extended potentiostatic electrolysis in 0.1 M TBAP solution in ACN. When the electrolysis was carried out with dry ACN (less than 10 ppm H_2O) the results show CO as being the main product, with a 42% faradaic efficient (on the basis of Eq 5 below). We also determined the electrolysis current vs. time curve with the aim of presenting quantitative information about the products formed and thus supporting the proposed mechanism (see below). The results obtained for 120-min electrolysis at an applied potential of -1.5 V in CO_2-purged 0.1 M TBAP/dry acetonitrile are shown in Figure S7. The corresponding *Q-t* curve is shown in Figure S8. The results of tungsten concentration estimated from the ICP-MS measurements and the amount of produced CO together with calculations based on the charge passed during electrolysis are presented in tables TS1 and TS2 as Supplementary data.

When the electrolysis was done in humid ACN (530 ppm H_2O as determined by Karl Fisher titration), formate and CO were determined as the main products. The determination of carbonate was attempted without positive results. This is likely due to the fact that both supporting electrolyte and carbonate have virtually identical retention times.[31] Figure S9 in the Supplementary data shows the chromatograms for the injection of CO_2 and CO patrons, and for either air or a 250 µl sample from the headspace of the working electrode compartment. Figure S10 shows ion chromatograms for the injection of oxalate and formate patrons as well as for the working solution after 1.5 h of electrolysis. The injection of the background signal for the supporting electrolyte is also given. Other techniques such as GC-MS were used and no additional reduction products such as methanol or methane were detected.

4. DISCUSSION

For the following discussion, it is important to keep in mind that under dry conditions, gas chromatography shows CO as being the main product with a faradaic efficiency of 42%. In our case, (bi)carbonate was not detected under the employed experimental conditions. In addition, ion chromatography and GC-MS techniques were used and other products were not detected.

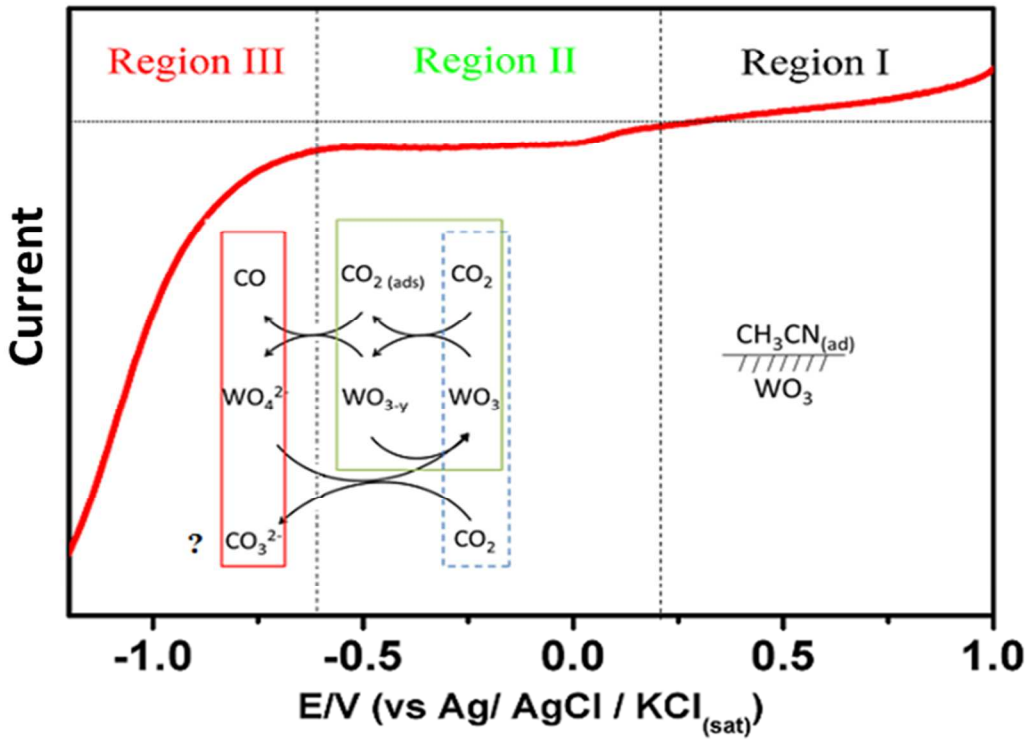

Scheme 1. Sketch of the adsorption, activation and reduction of CO_2 on WO_3 electrodes as a function of applied potential. Reduction and electrodissolution of WO_3 is also represented. The blue and red boxes indicate reactants and products, respectively. The green box refers to the species involved in the electrochromic effect.

The results obtained in this study show that there are several processes occurring in different potential regions that play an important role in CO_2 reduction on WO_3 electrodes. In scheme 1,

the CO_2 reduction process over a WO_3 electrode is sketched as a function of the region of applied potential. When the electrolyte is N_2-saturated, ACN molecules are adsorbed, being their surface density higher as the electrode is polarized to more negative potentials (region I) [39]. Region II corresponds to the development of capacitive currents associated with the appearance of electrochromic effects. In this respect, one should bear in mind that the tetrabutylammonium cation is more voluminous than the cavity available in WO_3 for intercalation, which is 0.52 nm in size.[25,44] This fact is important because with non-intercalating cations, a model for electrochromism with dissociative reduction of WO_3 has been considered. This mechanism entails a loss of mass (determined via electrochemical quartz crystal microbalance measurements),[45] due to the electrodissolution of WO_3 according to:

$$(1+x)WO_3 + 2x\,e \rightarrow WO_{3-x} + xWO_4^{2-} \qquad (2)$$

The partial electroreduction of tungsten atoms from W^{+6} to W^{+5} induce an oxygen deficient (oxygen vacancies) tungsten oxide lattice (WO_{3-x}) and electrodissolution of WO_4^{2-}.

In the presence of CO_2, the formation of oxygen vacancies caused by the application of increasingly negative potentials seems to be favored by the stabilization of W^{5+} species upon CO_2 chemisorption. Therefore, it is plausible to think that CO_2 can be adsorbed in W^{6+} sites and that the oxygen vacancy generation is favored. In this respect, XPS studies demonstrate that CO_2 adsorption on TiO_2 induce the generation of oxygen vacancies through carbonate formation [36]. The reduction of the metal is facilitated, provoking an enhancement of the capacitive currents in the CV profiles, even at potentials not causing CO_2 reduction. The adsorption of CO_2 would thus promote the generation of non-stoichiometric WO_{3-y} together with the formation of WO_4^{2-} species, according to

$$(1+\mathrm{y})\mathrm{WO_3} + \mathrm{yCO_2} + 2\mathrm{y\ e} \rightleftharpoons \mathrm{WO_{3-y}(CO_2)}_y + \mathrm{yWO_4^{2-}} \qquad (3)$$

Note that in Eqs. 2 and 3 $y>x$. In this dissociative model, the partial electroreduction of WO_3 is limited to the interfacial region, while no significant structural damage occurs in the underlying region of the WO_3 film. For this reason, the coefficient y has a relatively small value.[45] The fact that $y>x$ can be supported if one assumes that the adsorption of CO_2 on W^{5+} is stronger than on W^{6+}, inducing a stabilization of the W^{5+} sites. In this context, it is worth noting that research about the adsorption of CO_2 on Ti^{4+} and Ti^{3+} sites has been reported for TiO_2. The activation energy for CO_2 desorption from Ti^{4+} and Ti^{3+} sites was 48.5 kJ/mol and 54 kJ/mol, respectively. This suggest that Ti^{3+} sites bind CO_2 slightly more strongly than Ti^{4+} sites.[46] It is, thus reasonable to assume that the adsorption of CO_2 on W^{5+} sites is favored, which induces a stabilization of W^{5+} sites. Hence, a synergistic effect between CO_2 and the surface sites is verified. The adsorption of CO_2 not only activates the CO_2 molecule due to adduct formation, but also induces a promotion of oxygen vacancies associated with the existence of W^{5+}.

Upon lowering the applied potential further, the resulting high concentration of localized electrons in the near-surface region would facilitate charge transfer from the electrode to adsorbed CO_2 molecules leading to the appearance of faradaic currents (region III). The CO generation would be accompanied by the electrodissolution of WO_3 as WO_4^{2-} according to:

$$(1+\mathrm{y})\mathrm{WO_{3-y}(CO_2)}_y + 2ye \rightarrow \mathrm{WO_{3-y}} + \mathrm{yCO} + \mathrm{yWO_4^{2-}} \qquad (4)$$

The sum of eqs 3 and 4 would give the global equation for CO_2 reduction concomitant with a electrodissolution of WO_3 according to a dissociative electroreduction model:

$$\mathrm{yCO_2} + (1+2\mathrm{y})\mathrm{WO_3} + 4ye \rightarrow \mathrm{WO_{3-y}} + \mathrm{yCO} + 2\mathrm{yWO_4^{2-}} \qquad (5)$$

Eq 5 implies that there is WO_3 corrosion (WO_4^{2-} generation) tantamount to CO_2 reduction (CO generation). However, the amount of tungsten in solution present after potentiostatic electrolysis is three orders of magnitude lower than that calculated from the charge passed through the electrode (table TS1). This indicates that the WO_4^{2-} species is consumed in the presence of CO_2, in a process that can be written as:

$$WO_{3-y} + 2yWO_4^{2-} + yCO_2 \rightarrow (1+2y)WO_3 + yCO_3^{2-} + 2ye \qquad (6)$$

in which the regeneration of WO_3 is accompanied by carbonate formation, but interestingly decoupled of CO formation. Importantly, eqs. 5 and 6 show that the WO_3 electrode material act as a catalyst for CO_2 reduction decreasing the overpotential for CO_2 reduction not only by CO_2 activation through adsorption, but also acting as a mediator that offers a favorable chemical environment for CO_2 reduction. The WO_3 switching proposed in equations (5) and (6) leads to a continuous surface renovation (while keeping a high electronic density in surfaces states) that plays in favor of CO_2 reduction. However, the presence of tungsten traces in the working solution indicates that the rate of regeneration of WO_3 (Eq 6) is slightly slower than that of WO_4^{2-} formation (Eq 5). As a consequence of the continuous electrodissolution/deposition of tungsten oxide together with lattice polarization and deformation, drastic changes in the electrode morphology are expected upon electrolysis. In fact, Figure 7 shows FE-SEM images for a WO_3-NR electrode before and after electrolysis at -1.5 V for 1 h. These images provide evidence of the morphological changes that occur in the electrode due to tungsten oxide dissolution/deposition occurring during CO_2 reduction. Concretely, Figure 7a shows the initial electrode structure, formed by well-defined nanorods randomly oriented with diameters in the range 40-100 nm and an average length of 300 nm. In Figure 7b, a SEM image of the WO_3 electrode is shown after potentiostatic electrolysis. As observed, the density of small diameter

nanorods increases and there appear small nanoparticles with a more isotropic shape (see encircled zone). In addition, in some zones of the electrode the electrodissolution process predominates over regeneration leading to a drastic change in morphology (appearance of nanoparticle aggregates) and even to the partial exposure of the conducting glass substrate (Figure S11).

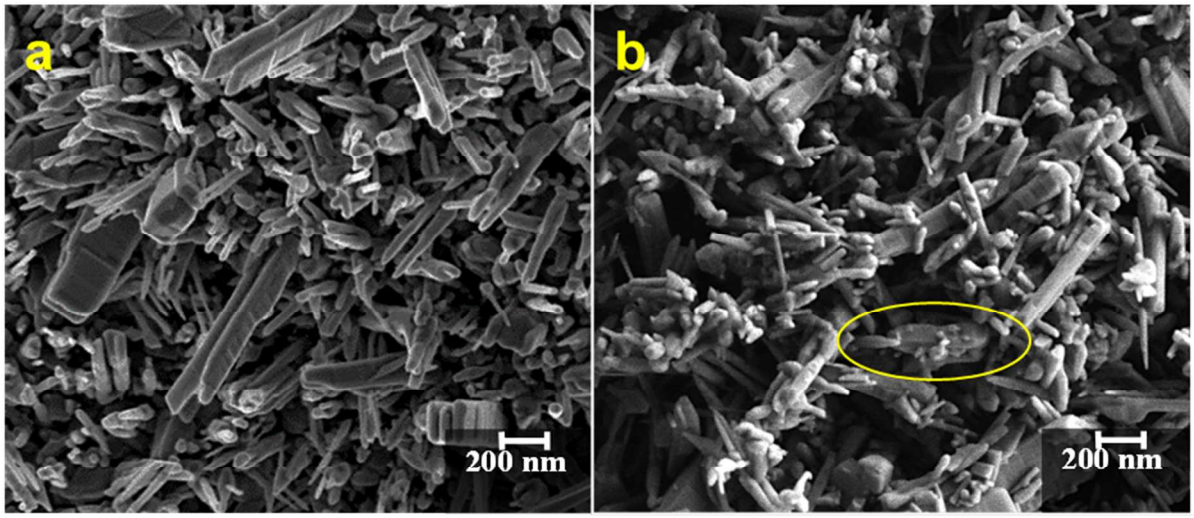

Figure 7. FE-SEM micrographs for a WO_3-NR/FTO electrode (a) before and (b) after potentiostatic electrolysis. Applied potential of -1.5 V for 1 hour in TBAP 0.1 M/dry acetonitrile.

The global reaction including WO_3 regeneration (Eqs. 5 + 6) would be that corresponding to the reductive disproportionation of CO_2. Admittedly the fact that the detection of CO_3^{2-} was not successful casts some doubts about CO_2 being the species accepting O^{2-} to regenerate the electrode material.

These considerations demonstrate that the presence of TBA^+ cations promotes a favorable behavior of WO_3 for CO_2 reduction. In fact, the presence of small cations being able to intercalate in the lattice of WO_3 while maintaining electroneutrality would inhibit the

electrodissolution process. In this way, the results of CO_2 reduction, using $LiClO_4$ as a supporting electrolyte in ACN, provide important evidence of the role of the WO_3 surface as an electrocatalyst in the CO_2 reduction. As mentioned above, the capacity of lithium to be adsorbed and intercalated is well known. When the system is saturated with N_2, characteristic signals of the formation of Li_xWO_3 blue-colored bronze species are shown.[43] In a CO_2-saturated solution, the increase in current response expected for CO_2 reduction is not obvious (Figure 4), which indicates that eq (3) is inhibited by Li^+ intercalation.

The mechanism presented above also helps rationalize the in situ UV/vis spectroelectrochemical measurements presented in Figure 6. Under potentiostatic control, the absorbance values in CO_2-purged solution are significantly higher than for the N_2-purged solution. When the electrode is maintained at open circuit the absorbance decay in the presence of CO_2 is observed to be faster than in the case of N_2, (the inset of Figure 6 shows normalized absorbance values for both N_2 and CO_2). This confirms the ability of CO_2 to be reduced by W^{5+} surface species in non-stoichiometric WO_{3-y}. In this case the oxygen deficiency is alleviated by oxygen from CO_2 molecules according to:

$$WO_{3-y}(CO_2)_y \rightarrow WO_3 + yCO \qquad (7)$$

It is worth noting that the value of y in Eq 7 will strongly depend on the applied potential. Only if y attains a sufficiently high value, the corresponding tungsten surface species are reductive enough as to trigger reaction 7. This assumption is supported by the results obtained by Hepel et al. showing that in aqueous solution, water reduction proceeds in a similar way, with H_2 formation and oxygen transfer to the oxide surface.[44,45,47] Interestingly, from the decay in absorbance as a function of time a rate law $d[WO_{3-y}]/dt = -k\,[WO_{3-y}]^{0.6}$ is obtained. This is

compatible with the order one expected from Eq (7) if we consider a rate constant whose values decrease with the concentration of WO_{3-y} as $k = k_0[WO_{3-y}]^{-0.4}$. This is equivalent to assume that the rate constant is potential dependent and that it decreases with increasing potential as expected for an electroreduction process. Of course, the decrease in absorbance of the samples is accompanied by an increase in the open circuit potential of the electrode. Not all the electrons accumulated in W^{5+} sites can be transferred, as only the electrons that have a potential more negative than the onset of CO_2 reduction (-0.7 V vs Ag/AgCl/KCl) have enough reductive power. After 600s of open circuit, potential and absorbance measurements were stopped and the electrode was maintained in the CO_2-purged solution for 24h. After this period of time the electrode still maintained a slight blue coloration. It should be borne in mind that the electrons involved in the reduction reaction are located at different energy levels within a surface states distribution. In scheme 2, a sketch of the electronic structure of both electrode and redox electrolyte is shown.

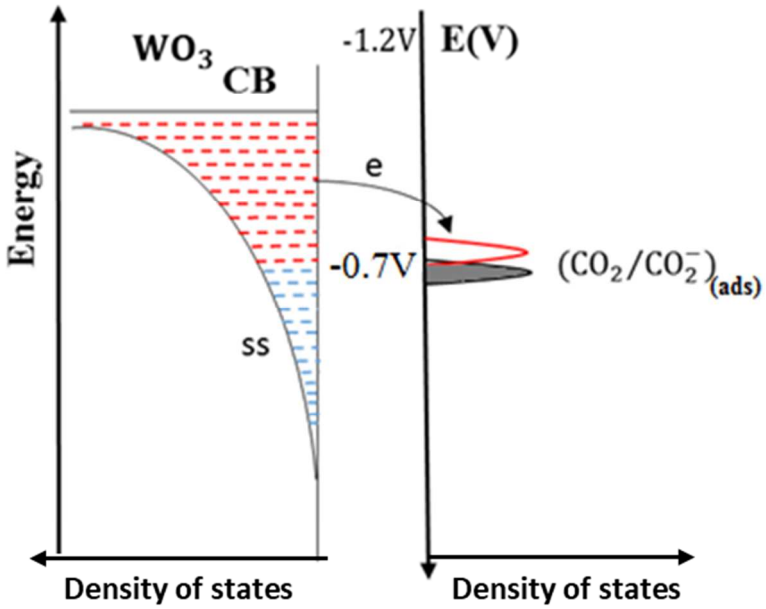

Scheme 2. Charge transfer from accumulated electrons in W^{5+} sites to CO_2 molecules. Blue region shows the electrons accumulated in WO_3 with potentials less negative than -0.7V, which cannot be transferred to adsorbed CO_2.

CO_2 reduction in ACN as a solvent is highly sensitive to trace amounts of water. A number of studies have been carried out in aprotic solvents and it is widely accepted that traces of water can change the reaction path.[26,48,49] In our case, the presence of water enhances the cathodic currents associated with CO_2 reduction. It has been described that in organic solvents such as dimethylformamide (DMF) or dimethyl sulfoxide (DMSO), the reaction begins with CO_2 activation and $CO_2^{\cdot-}$ formation, followed by the steps

$$CO_2^{\cdot-} + CO_2^{\cdot-} \rightarrow C_2O_4^{2-} \quad (8)$$

$$CO_2^{\cdot-} + CO_2 + e \rightarrow CO + CO_3^{2-} \quad (9)$$

$$CO_2^{\cdot-} + H_2O + 1e \rightarrow HCOO^- + OH^- \qquad (10)$$

that is, C-C coupling of two $CO_2^{\cdot-}$ radical anions with the formation of oxalate (Eq 8); C−O coupling of $CO_2^{\cdot-}$ and CO_2, leading to CO and CO_3^{2-} as products (Eq 9);[50] and through $CO_2^{\bullet-}$ electron-proton coupled transfer, yielding formate as the main reaction product (Eq 10).[48] In all the cases, the rate-determining step is the formation of the radical anion, which occurs at negative electrode potential.

On the other hand, under wet conditions, both formate and CO were detected by chromatographic techniques. In this case, formate generation could proceed according to Eq 10 for electron-proton coupled transfer from water traces present in the working solution. This confirms that the CO_2 reduction in ACN is highly sensitive to even residual amounts of water (from the ACN itself or the TBAP salt; 530ppm in this case). The formation of CO probably occurs upon water consumption near the electrode surface leading to local conditions similar to those of dry ACN. However, once again, carbonate formation was not detected by ion chromatography.

5. CONCLUSIONS

In summary, electrochemical and spectroelectrochemical measurement have been used to study CO_2 reduction on nanostructured WO_3 electrodes in both dry and humid ACN solutions. For the first time, a direct correlation between CO_2 reduction and an enhancement of the electrochromic effect is reported. It can be explained by the synergy existing between CO_2 adsorption and the formation of oxygen vacancies at the WO_3 surface. In such a way, the CO_2 adduct formation not only induces a decrease in overpotential for CO_2 reduction but also induces an increase in the concentration of electroreduced species WO_3-y. This is reflected in a parallel increase of the capacitance of the WO_3 electrode in the cyclic voltammogram and in an enhancement of the absorbance values even at potentials for which CO_2 reduction does not proceed.

The onset of CO_2 reduction is observed at -0.16 V vs NHE, showing that WO_3 can act as an electrocatalyst for CO_2 reduction. However, the current densities at potentials significantly negative to the onset potential are modest, probably because the mechanism entails dissolution/deposition of WO_4^{2-} units. In comparison with metal and TiO_2 electrodes from voltammetric scans for CO_2 reduction in acetonitrile media,[38,40] WO_3 electrodes shows a highest onset potential. On the other hand, a beneficial increase in the CO_2 reduction currents has been observed when residual mounts of water are present with the simultaneous formation of CO and formate.

The electrochemical and spectroelectrochemical studies presented here, point to the use of metal transitions oxides as potential cathodes for CO_2 reduction. Studies along these lines are currently under way in our laboratory and will be reported elsewhere.

6. ASSOCIATED CONTENT

Conversion of potentials measured against Ag/AgCl(s)/KCl(aq) to the SHE scale. Supplementary figures: XRD patterns for the WO_3 samples, cyclic voltammograms for a conducting glass (FTO) electrode in 0.1M TBAP/acetonitrile, linear voltammetric scans for WO_3 electrodes at 5 $mV \cdot s^{-1}$, cyclic voltammograms for WO_3 electrodes in aqueous 0.1 M $HClO_4$, chronoamperograms for FTO/WO_3-NP in 0.1 M TBAP/acetonitrile, absorption spectra for an FTO/WO_3-NR electrode in 0.1 M TBAP/acetonitrile purged with N_2 or CO_2, potentiostatic electrolysis profiles for a WO_3-NR electrode in a CO_2-purged 0.1 M TBAP/dry acetonitrile, gas-TPD chromatograms for CO detection, ion chromatograms for formate detection, additional electrode SEM image after electrolysis. Supplementary tables: Tungsten concentration in the potentiostatic electrolysis experiments and carbon monoxide amounts calculated from the charge passed in the potentiostatic electrolysis. This material is available free of charge via the Internet at http://pubs.acs.org.

AUTHOR INFORMATION

Corresponding Author

roberto.gomez@ua.es; *phone: +34 965903748*

ACKNOWLEDGMENT

We are grateful for the financial support of MINECO through project MAT2015-71727-R (FONDOS FEDER). N. E. M. R. acknowledges COLCIENCIAS National Doctoral Scholarship (567) and the Vicerrectorado de Investigación y Transferencia del Conocimiento de la Universidad de Alicante, A. K. D.-G. thanks the Mexican government (CONACYT) for the award of a doctoral grant.

REFERENCES

(1) Freund, H.-J.; Roberts, M. W. *Surf. Sci. Rep.* **1996**, *25*, 225-273.

(2) Indrakanti, V. P.; Kubicki, J. D.; Schobert, H. H. *Energy Environ. Sci.* **2009**, *2*, 745-758.

(3) Lamy, E.; Nadjo, L.; Savéant, J. M. *J. Electroanal. Chem. Interfacial Electrochem.* **1977**, *78*, 78-403.

(4) Koppenol, W. H.; Rush, J. D. *J. Phys. Chem.* **1987**, *91*, 4429-4430.

(5) Schwarz, H. A.; Dodson, R. W. *J. Phys. Chem.* **1989**, *93*, 409-414.

(6) Rasko, J.; Solymosi, F. *J. Phys. Chem.* **1994**, *98*, 7147-7152.

(7) Perissinotti, L. L.; Brusa, M. A.; Grela, M. A. *Langmuir* **2001**, *17*, 8422-8427.

(8) Hori, Y.; Kikuchi, K.; Suzuki, S. *Chem. Lett.* **1985**, *14*, 1695-1698.

(9) Berto, T. C.; Zhang, L.; Hamers, R. J.; Berry, J. F. *ACS Catal.* **2015**, *5*, 703-707.

(10) Ganesh, I. *Renew. Sustain. Energy Rev.* **2014**, *31*, 221-257.

(11) Tomita, Y.; Hori, Y.; T. Inui K. Izui, S. Yanagida and T. Yamaguchi BT - Studies in Surface Science and Catalysis, **1998**, 114, 581-584.

(12) Ogura, K.; Uchida, H. *J. Electroanal. Chem. Interfacial Electrochem.* **1987**, *220*, 333.

(13) Zhai, Q.; Xie, S.; Fan, W.; Zhang, Q.; Wang, Y.; Deng, W.; Wang, Y. *Angew. Chem.* **2013**, *125*, 5888-5891.

(14) Li, X.; Li, W.; Zhuang, Z.; Zhong, Y.; Li, Q.; Wang, L. *J. Phys. Chem. C* **2012**, *116*, 16047-16053.

(15) Liu, Y.; Huang, B.; Dai, Y.; Zhang, X.; Qin, X.; Jiang, M.; Whangbo, M.-H. *Catal. Commun.* **2009**, *11*, 210-213.

(16) Ulman, M.; Tinnemans, A. H. A.; Mackor, A.; Aurian-Blajeni, B.; Halmann, M. *Int. J. Sol. Energy* **1982**, *1*, 213-222.

(17) Kumar, B.; Llorente, M.; Froehlich, J.; Dang, T.; Sathrum, A.; Kubiak, C. P. *Annu. Rev. Phys. Chem.* **2012**, *63*, 541-569.

(18) Yamashita, H.; Shiga, A.; Kawasaki, S.; Ichihashi, Y.; Ehara, S.; Anpo, M. *Energy Convers. Manag.* **1995**, *36*, 617-620.

(19) Nguyen, T.-V.; Wu, J. C. S.; Chiou, C.-H. *Catal. Commun.* **2008**, *9*, 2073-2076.

(20) Froehlich, J. D.; Kubiak, C. P. *Inorg. Chem.* **2012**, *51*, 3932-3934.

(21) Takeda, H.; Koike, K.; Inoue, H.; Ishitani, O. *J. Am. Chem. Soc.* **2008**, *130*, 2023-2031.

(22) Habisreutinger, S. N.; Schmidt-Mende, L.; Stolarczyk, J. K. *Angew. Chem.* **2013**, *52*, 7372-7408.

(23) Xie, Y. P.; Liu, G.; Yin, L.; Cheng, H.-M. *J. Mater. Chem.* **2012**, *22*, 6746-6751.

(24) Somani, P. R.; Radhakrishnan, S. *Mater. Chem. Phys.* **2003**, *77*, 117-133.

(25) Hepel, M.; Redmond, H. *Cent. Eur. J. Chem.* **2009**, *7*, 234-245.

(26) Y., T.; S., T.; O., K.; Y., H. *J. Electrochem. Soc.* **2000**, *147*, 4164-4167.

(27) Hsiao, P.-T.; Chen, L.-C.; Li, T.-L.; Teng, H. *J. Mater. Chem.* **2011**, *21*, 19402-19409.

(28) Su, J.; Guo, L.; Bao, N.; Grimes, C. A. *Nano Lett.* **2011**, *11*, 1928-1933.

(29) Williams, D. B. G.; Lawton, M. *J. Org. Chem.* **2010**, *75*, 8351-8354.

(30) Kannan, R.; Kakade, B. A.; Pillai, V. K. *Angew. Chem. Int. Ed. Engl.* **2008**, *47*, 2653-2656.

(31) Voloschik, I. N.; Litvina, M. L.; Rudenko, B. A. *J. Chromatogr. A* **1994**, *671*, 249-252.

(32) Kalanur, S. S.; Hwang, Y. J.; Chae, S. Y.; Joo, O. S. *J. Mater. Chem. A* **2013**, *1*, 3479-3488.

(33) Batchelor, R. A.; Hamnett, A. Bockris, J. O., Conway, B. E., White, R. E., Eds.; Springer US: Boston, MA, 1992; 265-415.

(34) Pavlishchuk, V. V; Addison, A. W. *Inorganica Chim. Acta* **2000**, *298*, 97-102.

(35) Indrakanti, V. P.; Kubicki, J. D.; Schobert, H. H. *Fuel Process. Technol.* **2011**, *92*, 805-811.

(36) Bhattacharyya, K.; Danon, A.; K.Vijayan, B.; Gray, K. A.; Stair, P. C.; Weitz, E. *J. Phys. Chem. C* **2013**, *117*, 12661-12678.

(37) Yamamoto, M.; Yoshida, T.; Yamamoto, N.; Yoshida, H.; Yagi, S. *J. Surf. Sci. Nanotechnol.* **2014**, *12*, 299.

(38) Figueiredo, M. C.; Ledezma-Yanez, I.; Koper, M. T. M. *ACS Catal.* **2016**, *6*, 2382-2392.

(39) Rudnev, A. V.; Zhumaev, U. E.; Kuzume, A.; Vesztergom, S.; Furrer, J.; Broekmann, P.; Wandlowski, T. *Electrochim. Acta* **2016**, *189*, 38-44.

(40) Ramesha, G. K.; Brennecke, J. F.; Kamat, P. V. *ACS Catal.* **2014**, *4*, 3249-3254.

(41) Matsubara, Y.; Grills, D. C.; Kuwahara, Y. *ACS Catal.* **2015**, *5*, 6440-6452.

(42) Eckert, F.; Leito, I.; Kaljurand, I.; Kütt, A.; Klamt, A.; Diedenhofen, M. *J. Comput. Chem.* **2009**, *30*, 799-810.

(43) Buch, V. R.; Chawla, A. K.; Rawal, S. K. *Mater. Today Proc.* **2016**, *3*, 1429-1437.

(44) Hepel, M.; Dela-Moss, L. I.; Redmond, H. *J. Solid State Electrochem.* **2014**, *18*, 1251-1260.

(45) Hepel, M.; Wickham, D. In *ECS Transactions*; **2009**, *19*, 11-23.

(46) Xiong, L. Bin; Li, J. L.; Yang, B.; Yu, Y. *J. Nanomater.* **2012**, *2012*, 1-13.

(47) Shiyanovskaya, I.; Tewksburry, E.; Hepel, M. *J. New Mater. Electrochem. Syst.* **2000**, *3*, 241-247.

(48) Ikeda, S.; Takagi, T.; Ito, K. *Bull. Chem. Soc. Jpn.* **1987**, *60*, 2517-2522.

(49) Hori, Y.; Vayenas, C. G.; White, R. E.; Gamboa-Aldeco, M. E. *Modern Aspects of Electrochemistry*; 2008.

(50) Amatore, C.; Saveant, J. M. *J. Am. Chem. Soc.* **1981**, *103*, 5021-5023.

Table of Contents and Abstract Graphics